Angewandte Chemie
Eine Zeitschrift der Gesellschaft Deutscher Chemiker

Supporting Information

Manufacturing Single-Atom Alloy Catalysts for Selective CO_2 Hydrogenation via Refinement of Isolated-Alloy-Islands

S. Zou, Y. Liang, X. Zhang, Q. Gu, L. Wang, H. Sun, X. Liao, J. Huang*, A. R. Masri*

Supplementary Materials for

Manufacturing Single-atom Alloy Catalysts for Selective CO_2 Hydrogenation via Refinement of Isolated-alloy-islands

Sibei Zou* [a], Xingmo Zhang [b], Qinfen Gu [c], Yuhang Liang [b], Lizhuo Wang [b], Haoyue Sun [b], Chunjing Su [b], Xiaozhou Liao [a], Jun Huang* [b], and Assaad R. Masri [a]

[a] School of Aerospace, Mechanical and Mechatronic Engineering, The University of Sydney, New South Wales 2006, Australia

[b] School of Chemical and Biomolecular Engineering, The University of Sydney, New South Wales 2006, Australia

[c] Australian Synchrotron, 800 Blackburn Rd Clayton, Victoria, 3168, Australia

* Corresponding authors

Contents

1. Methods…….....……2

2. Supporting Figures and Tables…….7

Author Contributions and Notes…….23

References……..24

Methods

Preparation of Catalysts

The anatase-TiO_2, $NiCl_2 \cdot 6H_2O$, and $RuCl_3 \cdot xH_2O$ chemicals were purchased from Sigma-Aldrich (Australia) and used without further purification. Deionized water was used as a solvent in the entire experimental process. TiO_2 support was selected here because it has been widely proved to be an excellent reducible support for promoting the homogeneous RuNi alloy formation due to the H_2-spillover effect[1-4]. We have fixed the Ru/Ni atom ratio at 1/4 (weight ratio equals to 2/5), which was evidenced as the optimal atom ratio for RuNi homogeneous alloyed structures[2]. The effects of supports have also been eliminated by using the same pure anatase-TiO_2.

The $RuNi/TiO_2$ catalysts with different sizes were synthesis by one-step wetness impregnation through controlling the bimetallic loadings. To guarantee the formation of homogeneous alloys, catalysts were all fixed with the Ru/Ni atom ratio, which equals to a weight ratio of 2/5, according to previous studies[2]. In a typical procedure, TiO_2 (anatase, 1g) support was mixed with 20 mL aqueous solution containing a certain amount of $RuCl_3 \cdot xH_2O$ and $NiCl_2 \cdot 6H_2O$. The amount of the precursors was calculated according to the different metal loadings, as shown in Table. S1. After stirring the mixture under room temperature for 15 min, the suspension further slowly evaporated in a water bath (70 °C) with continually stirring for 12 h. The obtained solids were dried in the oven at 70 °C overnight and grounded into fine powders with mortar. Finally, the obtained powder was reduced under a flow of 20% H_2/N_2 (60 mL/min, 500 °C) for 2 h and then labelled as Ru_xNi_y/TiO_2 (x=metal loading of Ru, y=metal loading of Ni).

Table. S1 Catalysts synthesis parameters.

Sample Label	Bimtallic loadings (wt%)	Ni (wt%)	Ru (wt%)	Ru/Ni weight ratio
$Ru_{0.5}Ni_{1.25}$	1.75	1.25	0.5	
$Ru_1Ni_{2.5}$	3.5	2.5	1	2/5
Ru_2Ni_5	7	5	2	

$Ru_3Ni_{7.5}$	10.5	7.5	3
Ru_4Ni_{10}	14	10	4
$Ru_5Ni_{12.5}$	17.5	12.5	5
Ru_6Ni_{15}	21	15	6

Catalyst characterizations: The single-atoms on the isolated nanoalloy-islands can be identified under the size of ~1 nm by the advanced high space-time resolution characterization techniques, including STEM-HADDF with double spherical aberration corrected, in-situ Diffuse reflectance infrared Fourier transform spectroscopy (DRIFTS) probed by CO molecules, and the synchrotron X-ray adsorption fine structure (XAFS).

The crystalline structure of catalysts was determined by X-ray diffraction (XRD). XRD patterns were recorded with PANalytical XPert Powder diffractometer using the Cu Kα radiation (45 kV and 40 mA, $\lambda = 1.5405$ Å). Before the XRD measurements, the catalysts were reduced at specific temperatures. Scans were taken 2θ range from 20° to 90° at a step size of 3.5°/min.

The atom-scale structure and nanoparticle size of catalysts were examined using the STEM-HAADF on an FEI Themis-Z double spherical aberration corrected S/TEM and FEI Spectra S/TEM both working at 300 kV. In accordance with established definitions, in this article we designate the 'nanoparticles' as bimetallic sizes > 1nm, while 'nanoclusters' as bimetallic sizes within 1 nm (≤ 1 nm) [5,6].The elemental mapping and distribution were determined by both the Energy Dispersive Spectroscopy (EDS), operated in the FEI Themis-Z S/TEM. The inverse Fast Fourier Transform (IFFT) images were processed by Gatan DigitalMicrograph 3.5 software. The samples were all first reduced at specific temperatures and suspended into ethanol with an ultrasonic dispersion for around 20 min. Then the suspension was deposited onto a carbon-film-coated copper grid and dried in the air at 80 °C for 10 min before the TEM/STEM investigation.

X-ray photoelectron spectroscopy (XPS) measurements were performed to determine the electron transfer and valence of elements with a Thermo Fisher ESCALAB 250Xi spectrometer with a focus monochromatic Al Kα radiation source. The binding energy was calibrated by the C1s peak of contamination carbon (284.8 eV) as a reference. Before the XPS measurements, the catalysts were reduced at specific temperatures.

The synchrotron X-ray adsorption spectra (XAS) measurements at Ru K-edge and Ni K-edge were conducted at the beamline in the Australian Synchrotron (ANSTO). The XAS spectra of all catalysts were collected in fluorescence mode. The Ru foil, RuO_2, Ni foil, and NiO were used as standard reference samples. All of the XAS spectra data were analysed through the IFEFFIT package (0.9.26 version) for data reduction (Athena) and data analysis (Artemis) [7].

DRIFTS: DRIFTS experiments were performed to investigate the surface intermediates during reaction under the steady-state or transition-state. The in-situ DRIFTS experiments were conducted in a high-temperature reaction chamber with ZnSe windows mounted inside a Thermo Scientific Nicolet iS50-FT-IR spectrometer equipped with an MCT detector chilled in liquid nitrogen. In a typical procedure, around 50 mg of undiluted catalysts in powder form were packed smoothly in the sample tank within the reaction chamber. Each spectrum data was collected at a resolution of 4 cm^{-1} with 32 scans, resulting in a collection rate of one spectrum every 19 seconds. All samples were reduced at 500 °C (under the flow of 20% H_2/N_2, 60 sccm for 2 h) before in-situ DRIFTS measurements.

CO DRIFTS: The CO chemisorption DRIFTS were conducted under room temperature (30 °C). Prior to the CO adsorption, all samples were in-situ activated with 20% H_2/N_2 (60 sccm) in the reactor cell at 500 °C for 30 min followed by purging with Ar (50 sccm) at the same temperature for 1 h to remove the surface adsorbed H_2. After the temperature cooled down to 30 °C under the Ar flow, the background spectrum was collected. Then the CO gas was purged into the reactor cell for 15-20 min, with spectra collected until a steady state reached. Following the CO adsorption at room temperature, Ar was purged through the reactor cell to remove the gas phase CO. All CO-DRIFTS spectra of catalysts are collected with no further changes observed.

CO desorption (without H_2) / dissociation (with H_2) in-situ DRIFTS: Prior to the CO adsorption, all samples were in-situ activated with 20% H_2/N_2 (60 sccm) in the reactor cell at 500 °C for 30 min followed by purging with Ar (50 sccm) at the same temperature for 1 h to remove the surface adsorbed H_2. After the temperature cooled down to 30 °C under the Ar flow, the background spectrum was collected. Then the CO gas was purged into the reactor cell for 15-20 min, with spectra collected until a steady state reached. Following the CO adsorption at room temperature, Ar was purged through the reactor cell, with spectra collected with no further changes observed. For CO desorption in-situ DRIFTS experiments, the cell was then heated under Ar flow at the temperature range of 30 – 250 °C, with spectra collected with no further change at every specific temperature (30, 50, 150, 200, and 250 °C). For CO dissociation in-situ DRIFTS experiments, the cell was then heated under 10% H_2/Ar flow at the temperature range of 30 – 300 °C, with spectra collected with no further change at every specific temperatures (30, 50, 150, 200, 250, and 300 °C).

CO_2 dissociation (without H_2) in-situ DRIFTS: To study the CO_2 dissociation active sites, CO_2 dissociation in-situ DRIFTS were conducted on Ru/TiO_2, Ni/TiO_2, and TiO_2 by introducing 5% CO_2 in N_2 at the temperature ranges of 80 – 450 °C. The spectra were obtained at each specific temperature after stabilization for 30 min to reach an equilibrium state of the reaction. Prior to the reaction, all samples were in-situ pre-treated with 20% H_2/N_2 (60 sccm) in the reactor cell at 500 °C for 30 min followed by purging with Ar (50 sccm) at the same temperature for 1 h. After the temperature cooled down to room temperature under the same Ar flow, the background spectrum was collected. Then the feed gas 5% CO_2 in N_2 (20 sccm) was introduced into the reactor cell, and the temperature was increased up to 450 °C in steps of 50 °C.

Steady-state reaction in-situ DRIFTS: The steady-state operando in-situ DRIFTS experiments were conducted under reaction conditions at different temperatures. The spectra were obtained at each specific temperature after stabilization for 30 min to reach an equilibrium state of the reaction. Prior to the reaction, all samples were in-situ pre-treated with 20% H_2/N_2

(60 sccm) in the reactor cell at 500 °C for 30 min followed by purging with Ar (60 sccm) at the same temperature for 1 h. After the temperature cooled down to room temperature under the same Ar flow, the background spectrum was collected. Then the feed gas mixture (CO_2/H_2=1/4, balanced with N_2) was introduced into the reactor cell, and the temperature was increased up to 450 °C in steps of 50 °C.

Transition-state reaction in-situ DRIFTS: To study the evolution of surface species over catalysts at the beginning of the reaction, transient experiments were conducted by alternatively switching the adsorption gas three times to first 5% CO_2 in N_2, then 20% H_2 in N_2, and finally 5% CO_2 in N_2 again. The experiments were performed at starting temperature of the catalytic reaction (250 °C for Ru_4Ni_{10}/TiO_2, and 350 °C for $Ru_1Ni_{2.5}/TiO_2$) according to the activity tests, with the low concentration of gas phase product and unstable surface species, which could be observed more clearly and distinguish bystander species. Prior to the reaction, all samples were in-situ pre-treated with 20% H_2/N_2 (60 sccm) in the reactor cell at 500 °C for 30 min followed by purging with Ar (60 sccm) at the same temperature for 1 h. The background spectrum was collected at the starting temperature of catalytic reaction (250 °C for Ru_4Ni_{10}/TiO_2, and 350 °C for $Ru_1Ni_{2.5}/TiO_2$) under the same Ar flow. Then the specific adsorption gas was introduced in sequence into the reactor cell and stabilized for 30 min every time after switching the feed gas. The spectra were collected continuously for 30 min during each adsorption procedure.

DFT Calculation Method

The spin-polarized DFT[8] calculations were carried out using the Vienna ab initio simulation package (VASP) [9]. The Perdew-Burke-Ernzerhof (PBE) [10] form of the generalized gradient approximation (GGA) was employed for describing the exchange and correlation functional, and the spin-orbit coupling (SOC) was included. The Grimme's D3 scheme[11] was adopted for describing van der Waals (vdW) interactions. Projector augmented wave (PAW) pseudopotentials were used to model the valence states and the interactions between core and valence electrons[12], where the kinetic energy cutoff for basis functions was set at 500 eV with a Monkhorst – Pack sampling of $8 \times 8 \times 8$ k-point grid for Ni unit cell and of $2 \times 2 \times 1$ k-point grid for the surface calculations. The alloy Ni (111) surface model was constructed by 3×3 slab of 4 layers separated by 20 Å of vacuum in periodic cells. The geometries were fully relaxed until the forces on each atom are less than 0.01 eV/Å. The adsorption energies were calculated by the following equation: $E_{ads} = E_{system} - (E_{slab} + E_{CO})$, where E_{system} stands for the total energy of optimized adsorption system, E_{slab} for the total energy of bare slab, and E_{CO} for the energy of CO.

Catalytic Activity Tests

Catalysts were all in-situ reduced at 500 °C under a flow rate of 60 mL/min of 20% H_2/N_2 for 2 h. The catalysts were evaluated in a continuous-flow quartz fixed bed micro-reactor (length=500mm, e.d.=9.0 mm, wall thickness=1.0 mm) under atmospheric pressure at a steady state for CO_2 hydrogenation. In a typical procedure, 100 mg catalysts were filled into the quartz reactor with quartz wool at both ends of the catalysts bed to stabilize the catalysts. The reactant gas mixture (5% CO_2 : 20% H_2 : 75% N_2) was fed into the reactor at a constant WHSV (Weigh Hourly Space Velocity) of 37,800 $mL \cdot g^{-1} \cdot h^{-1}$. The effluent gas products were passed through a dryer to remove water vapor. The concentration of reactant and product in outlet gases were continuously analysed by an on-line gas chromatograph (Agilent, 7890B GC System) equipped

with a TCD detector, using Ar as carrier gas. The CO_2 conversion and product selectivity (CH_4 and CO selectivity) for CO_2 hydrogenation reactions were calculated as the following equations:

$$CO_2\ Conversion\ (\%) = \frac{n(CO_2, inlet) - n(CO_2, outlet)}{n(CO_2, inlet)} \times 100\%$$

$$CH_4\ Selectivity\ (\%) = \frac{n(CH_4, outlet)}{n(CO, outlet) + n(CH_4, outlet)} \times 100\%$$

$$CO\ Selectivity\ (\%) = 100\% - CH_4\ Selectivity\ (\%)$$

$$CO_2\ Conversion\ Rate\left(mol_{CO_2} \cdot g_{NiRu}^{-1} \cdot min^{-1}\right) = \frac{F(CO_2, inlet) \times CO_2\ Conversion\ (\%)}{m(cat._{RuNi}, g)}$$

$$CO_2\ Converted\ to\ CO\ Rate\left(mol_{CO_2} \cdot g_{NiRu}^{-1} \cdot min^{-1}\right) = CO_2\ Conversion\ Rate\left(mol_{CO_2} \cdot g_{NiRu}^{-1} \cdot min^{-1}\right) \times CO\ Selectivity\ (\%)$$

Where n(CO_2, inlet) and n(CO_2, outlet) are the molar concentration of CO_2 in the feed and effluent gas, n(CH_4, outlet) are the molar concentration of CH_4 products in the outlet gas, n(CO, outlet) are the molar concentration of CO products in the outlet gas, F(CO_2, inlet) is the molar flow rate of CO_2 in the feed gas, and m($cat._{RuNi}$, g) is the mass of the active metal RuNi in catalysts.

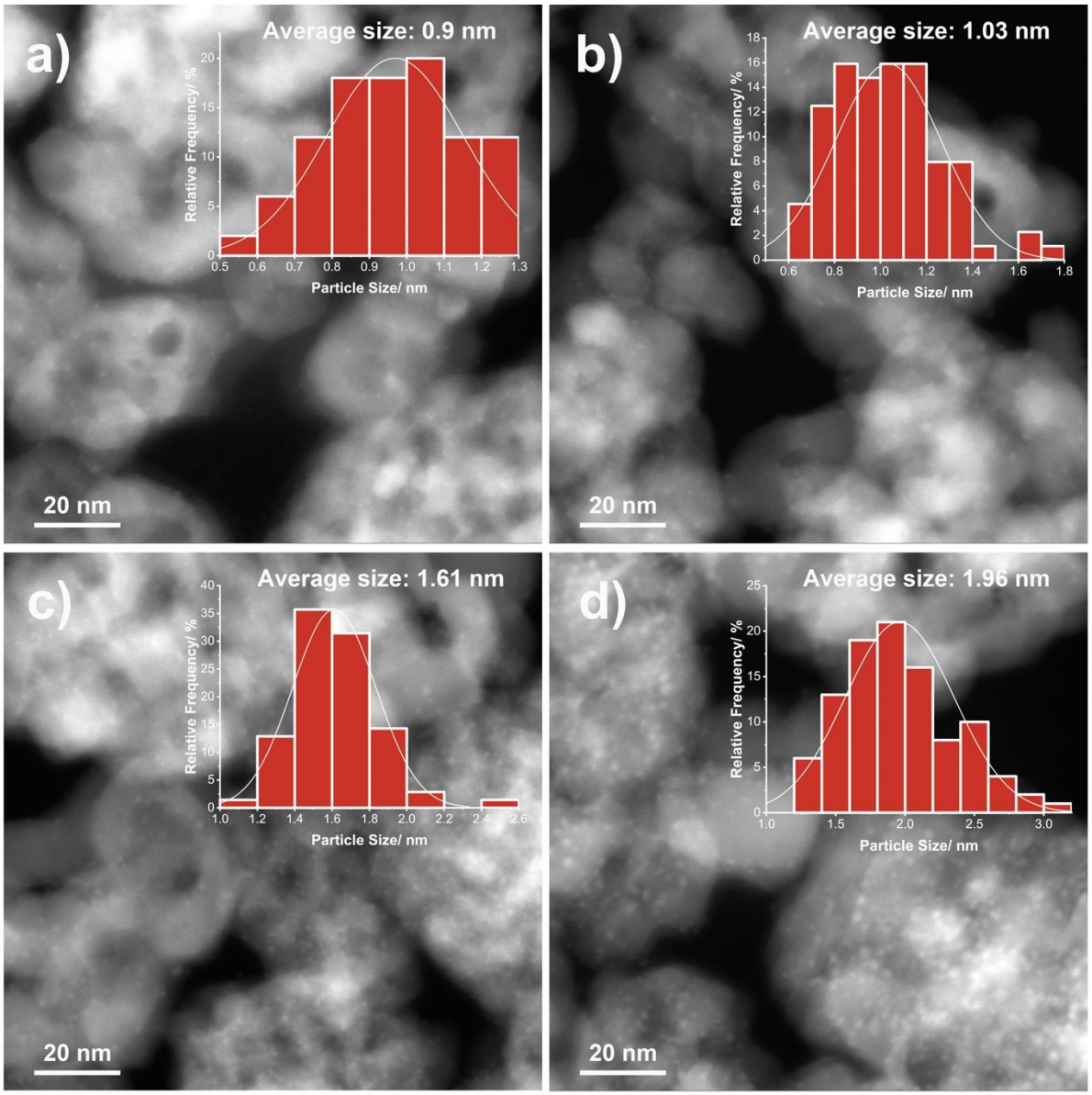


Fig. S1.

The bimetallic particle sizes calculated in STEM-HADDF of (a) $Ru_{0.5}Ni_{1.25}/TiO_2$, (b) $Ru_1Ni_{2.5}/TiO_2$, (c) Ru_2Ni_5/TiO_2, and (d) $Ru_3Ni_{7.5}/TiO_2$.

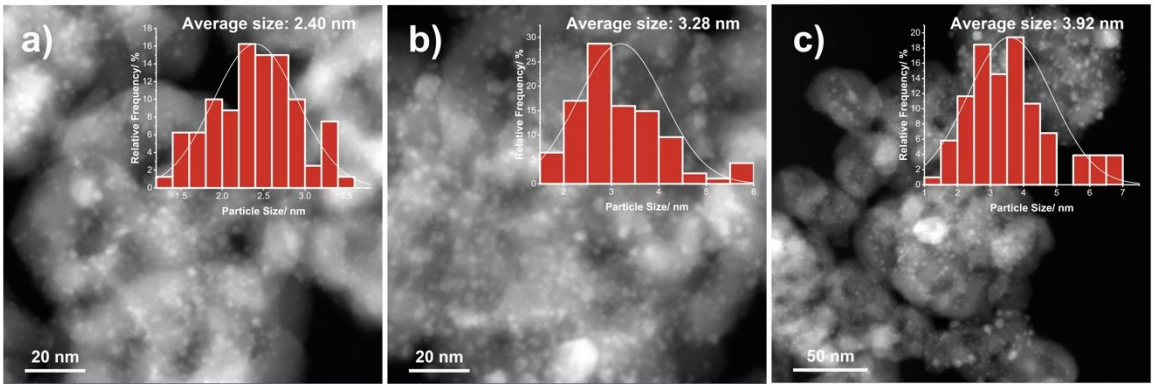


Fig. S2.

The bimetallic particle sizes calculated in STEM-HADDF of (a) Ru_4Ni_{10}/TiO_2, (b) $Ru_5Ni_{12.5}/TiO_2$, and (c) Ru_6Ni_{15}/TiO_2.

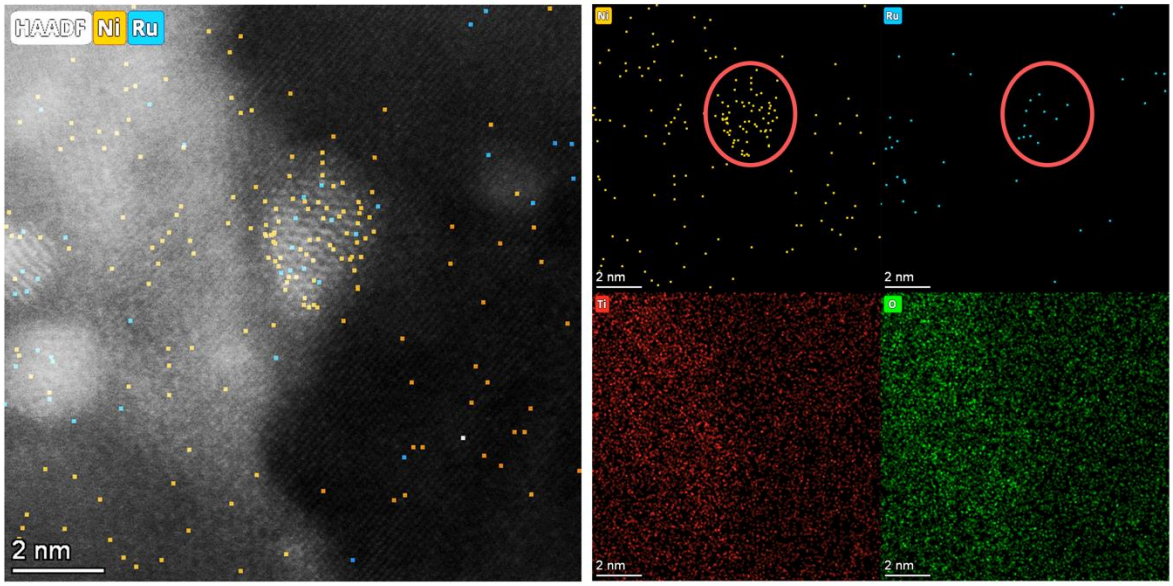


Fig. S3.

The STEM-HAADF and EDS mapping of $Ru_1Ni_{2.5}/TiO_2$.

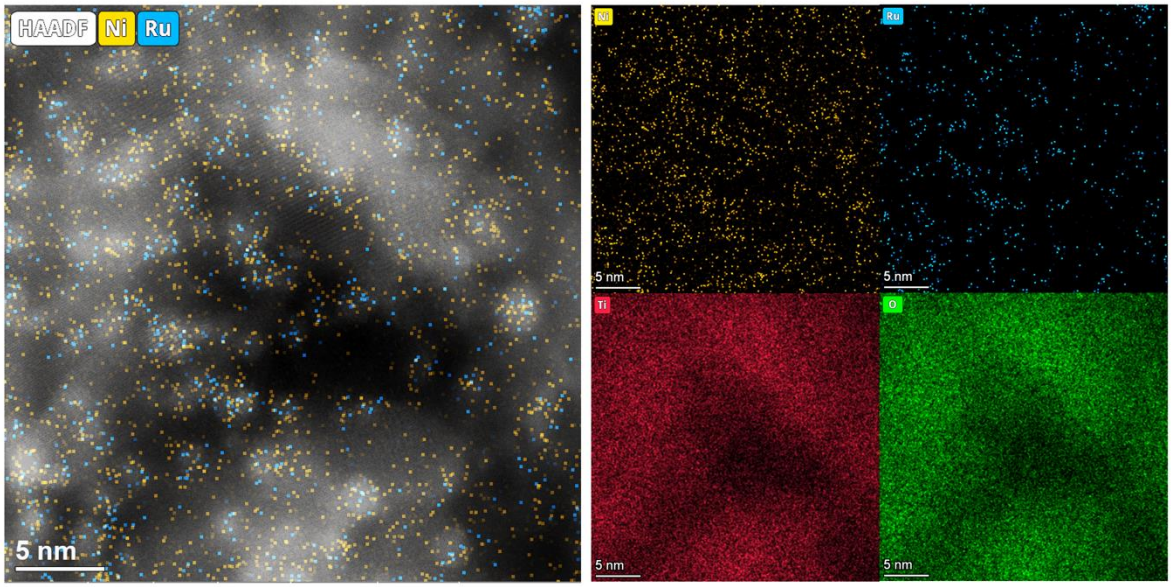


Fig. S4.

The STEM-HAADF and EDS mapping of Ru_4Ni_{10}/TiO_2.

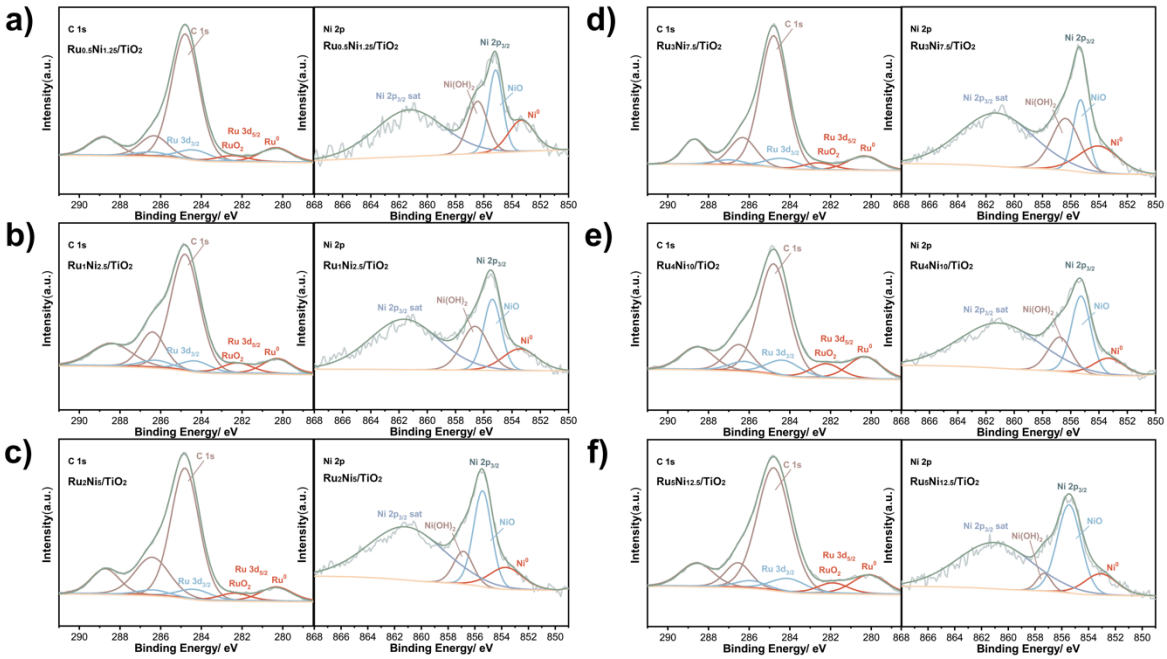


Fig. S5.

C 1s (Ru 3d) and Ni 2p XPS results of all catalysts: (a) $Ru_{0.5}Ni_{1.25}/TiO_2$, (b) $Ru_1Ni_{2.5}/TiO_2$, (c) Ru_2Ni_5/TiO_2, (d) $Ru_3Ni_{7.5}/TiO_2$, (e) Ru_4Ni_{10}/TiO_2, and (f) $Ru_5Ni_{12.5}/TiO_2$.

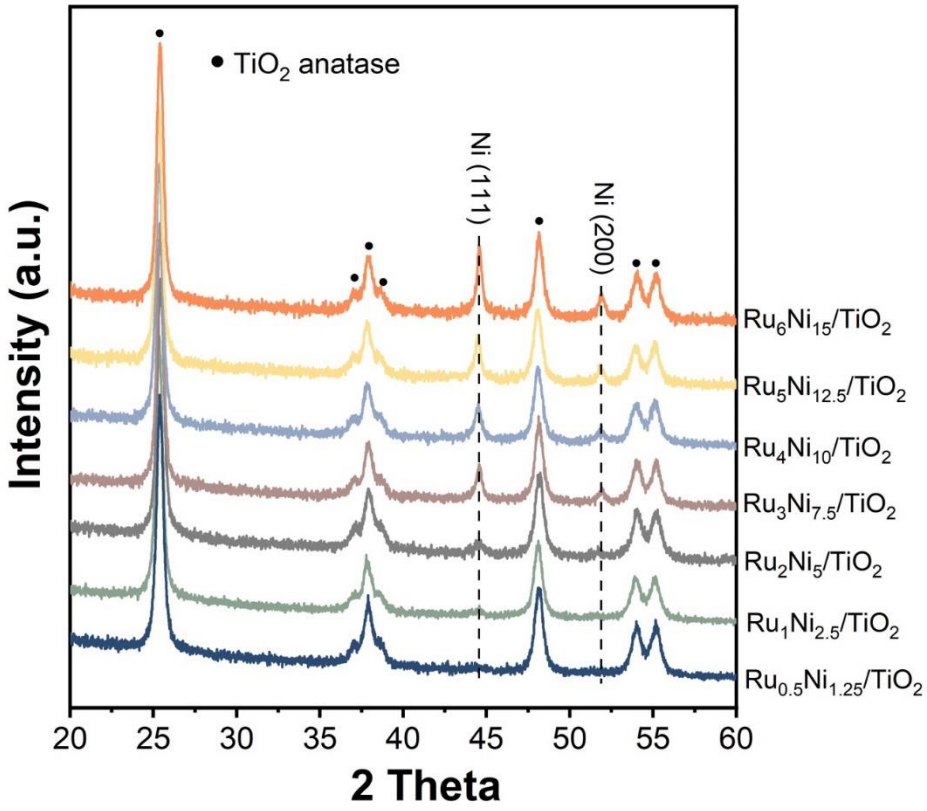


Fig. S6.

XRD results of all catalysts.

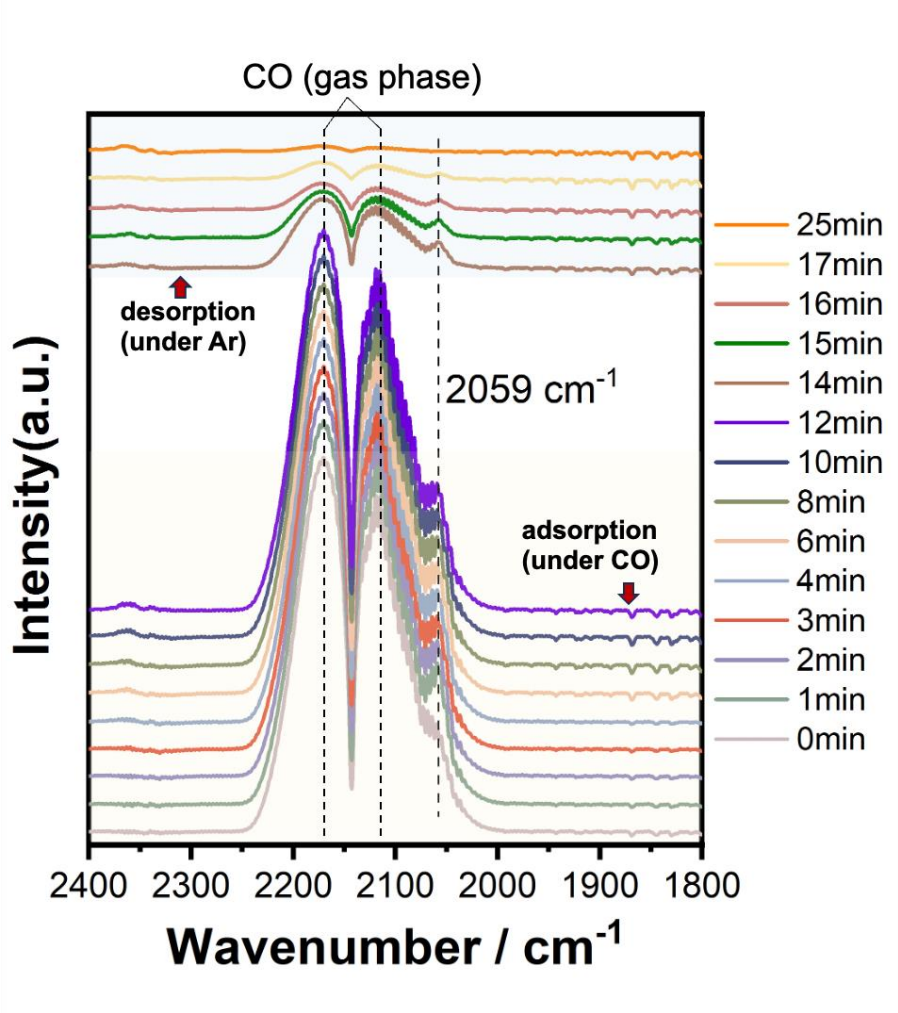


Fig. S7.

The CO-DRIFTS of Ni/TiO_2 from adsorption under CO to desorption under Ar.

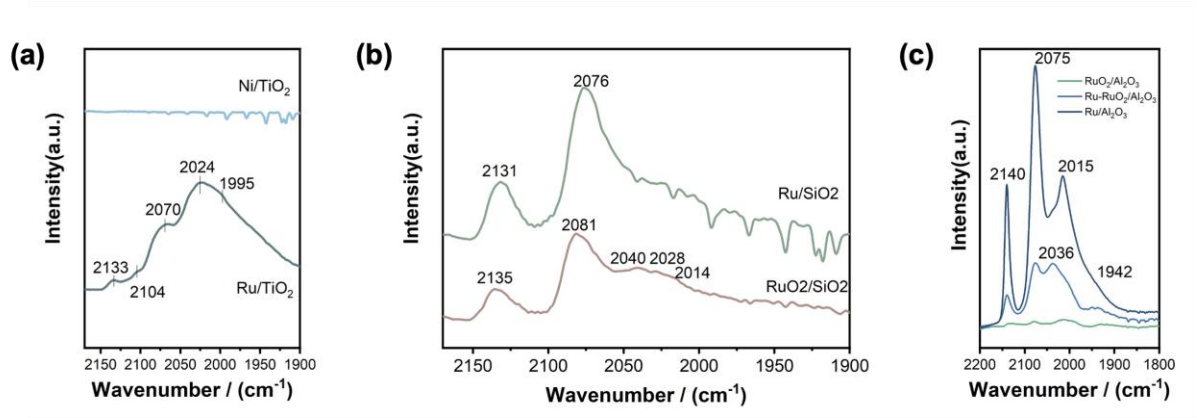


Fig. S8.

CO-DRIFTS of (a) Ru/TiO_2 and Ni/TiO_2; (b) Ru/SiO_2 and RuO_2/SiO_2; (c) Ru/Al_2O_3, $Ru\text{-}RuO_x/Al_2O_3$, and RuO_x/Al_2O_3.

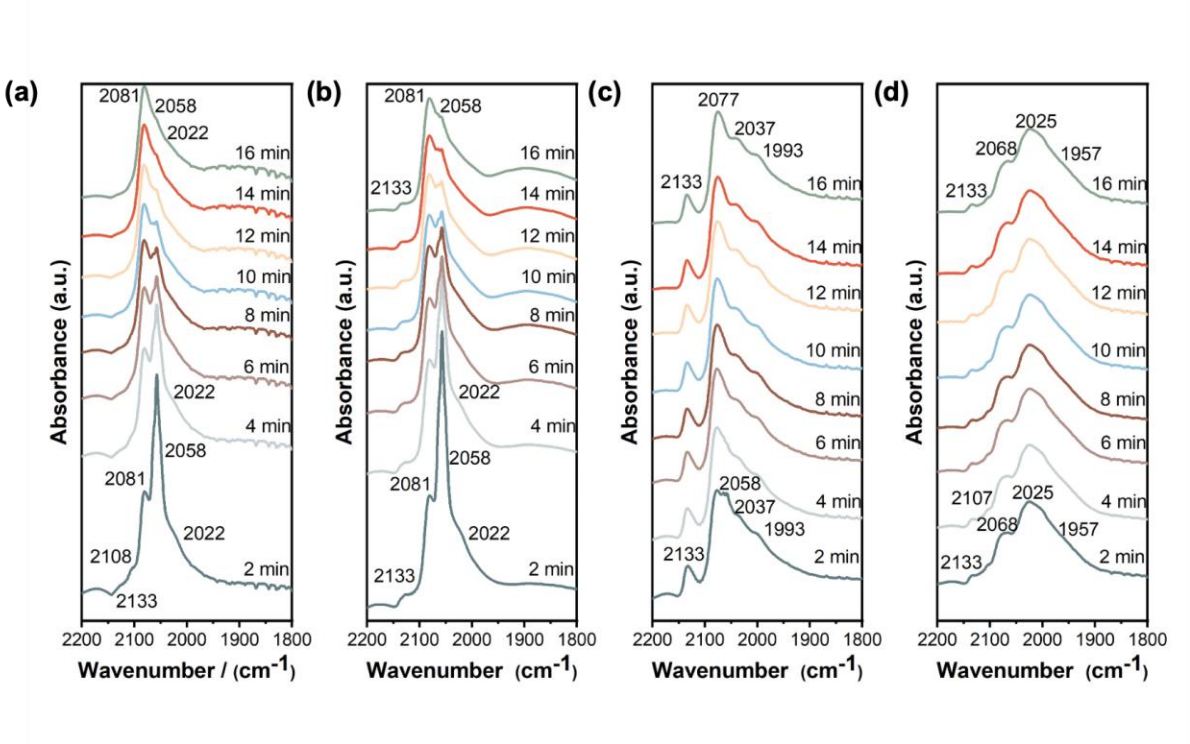


Fig. S9.

The time resolution in-situ experiment of CO-DRIFTS on (a) $Ru_1Ni_{2.5}/TiO_2$, (b) Ru_2Ni_5/TiO_2, (c) Ru_4Ni_{10}/TiO_2, and (d) Ru/TiO_2 catalysts (after no gas phase CO detected).

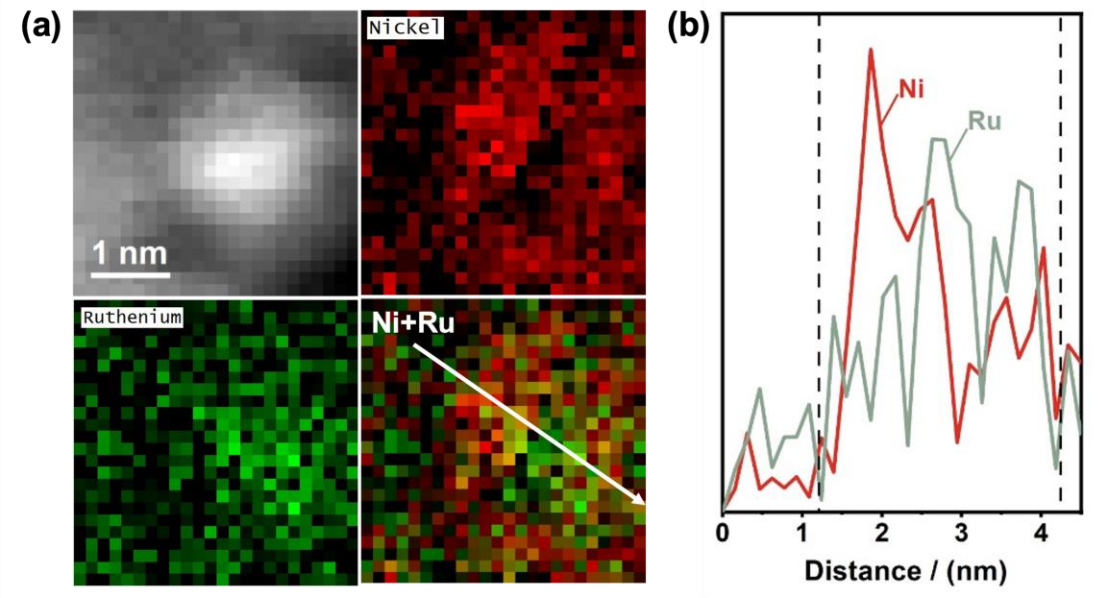


Fig. S10.

(a) The EELS mapping of Ni, Ru, and Ni+Ru of one specific nanoparticle in Ru_4Ni_{10}/TiO_2; (b) the corresponding line analysis of the EELS mapping in the direction of the white arrow in (a).

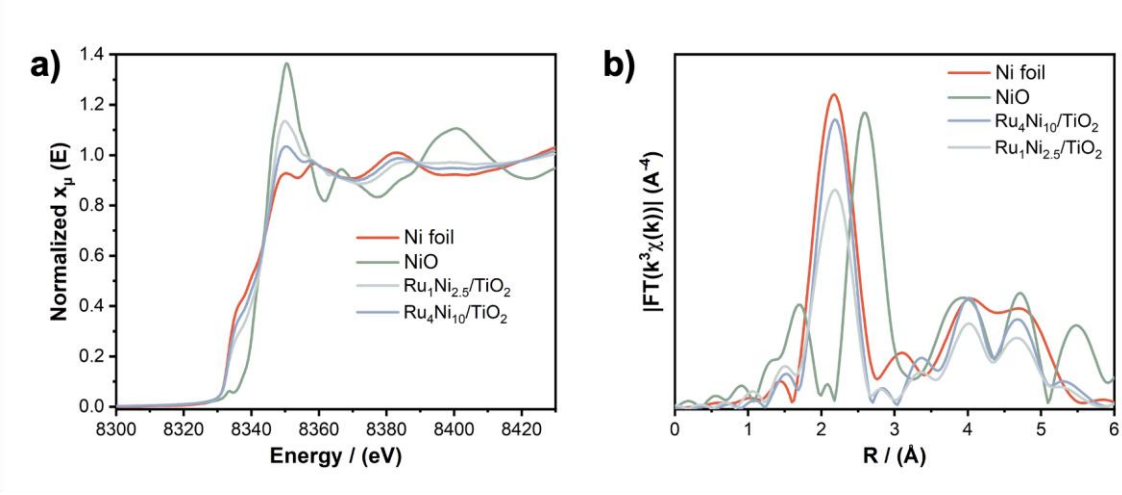


Fig. S11.

(a) Ni K-edge XANES for $Ru_1Ni_{2.5}/TiO_2$, Ru_4Ni_{10}/TiO_2, Ni foil, and NiO; (b) Ni K-edge EXAFS

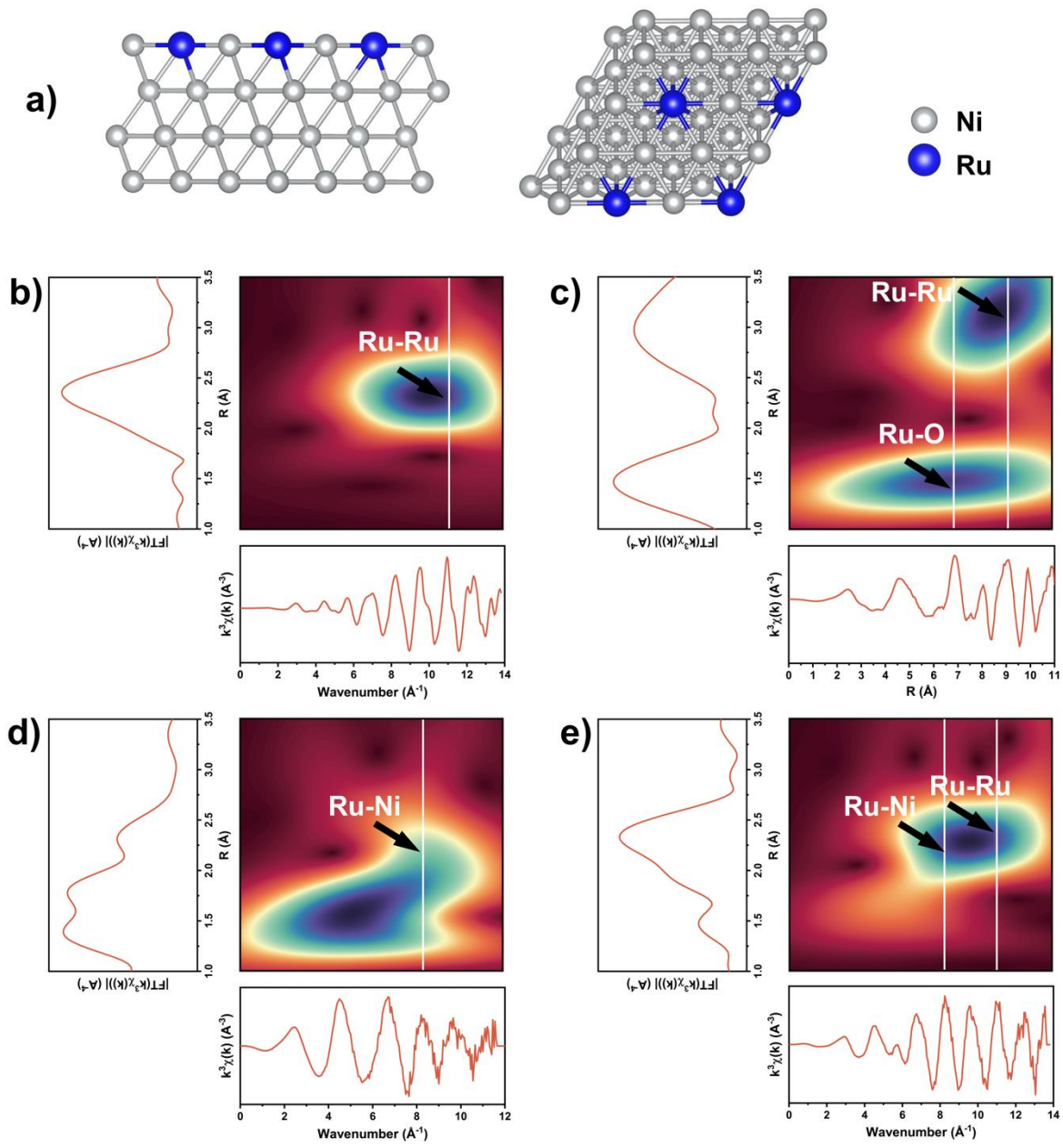


Fig. S12.

(a) schematic of CO adsorption configurations on cluster Ru site (top) and single Ru site (bottom) on NiRu alloy;the k^3-weighted wavelet transform with Morlet Function for the Ru k-edge of (b) Ru foil, (c) RuO_2, (d) $Ru_1Ni_{2.5}/TiO_2$, and (e) Ru_4Ni_{10}/TiO_2. (All the Ru foil and RuO_2 samples in the figures are standard samples as reference.)

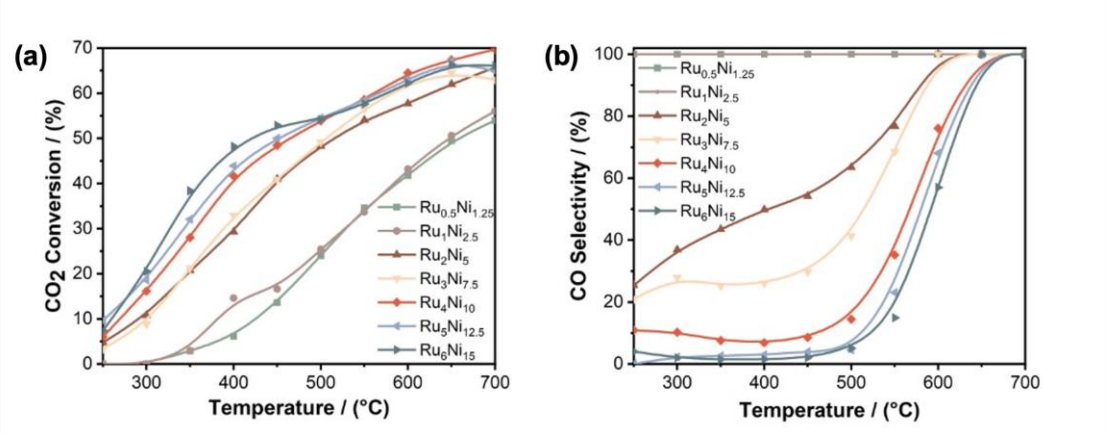


Fig. S13.

(a) The CO_2 conversion of all different catalysts under 250-700 °C; (b) the CO selectivity of all different catalysts under 250-700 °C.

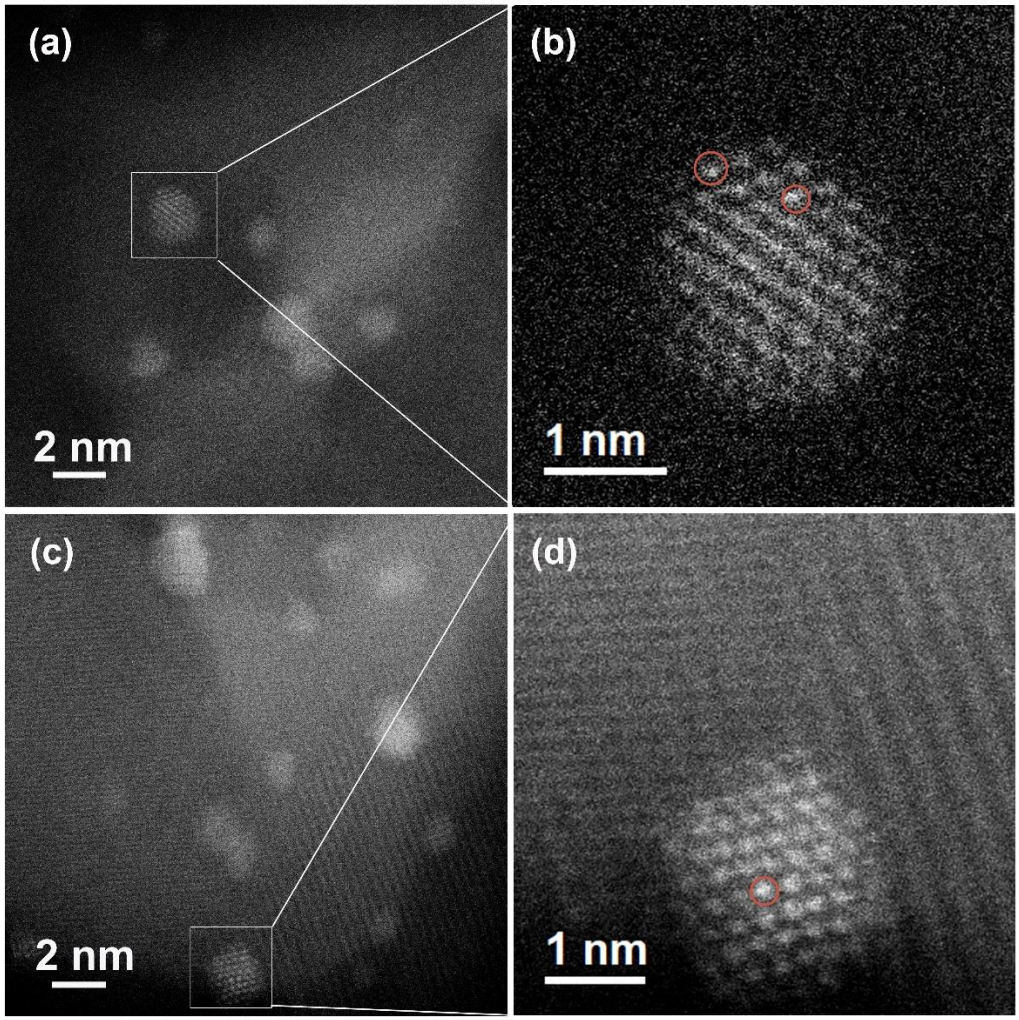


Fig. S14.

(a) The high-magnification STEM-HAADF of Ru_1Ni_{10}/TiO_2 and the (b) corresponding atomic resolution STEM-HAADF of one nanoparticle of Ru_1Ni_{10}/TiO_2. (c) The high-magnification STEM-HAADF of another area of Ru_1Ni_{10}/TiO_2 and the (d) corresponding atomic resolution STEM-HAADF of another nanoparticle of Ru_1Ni_{10}/TiO_2.

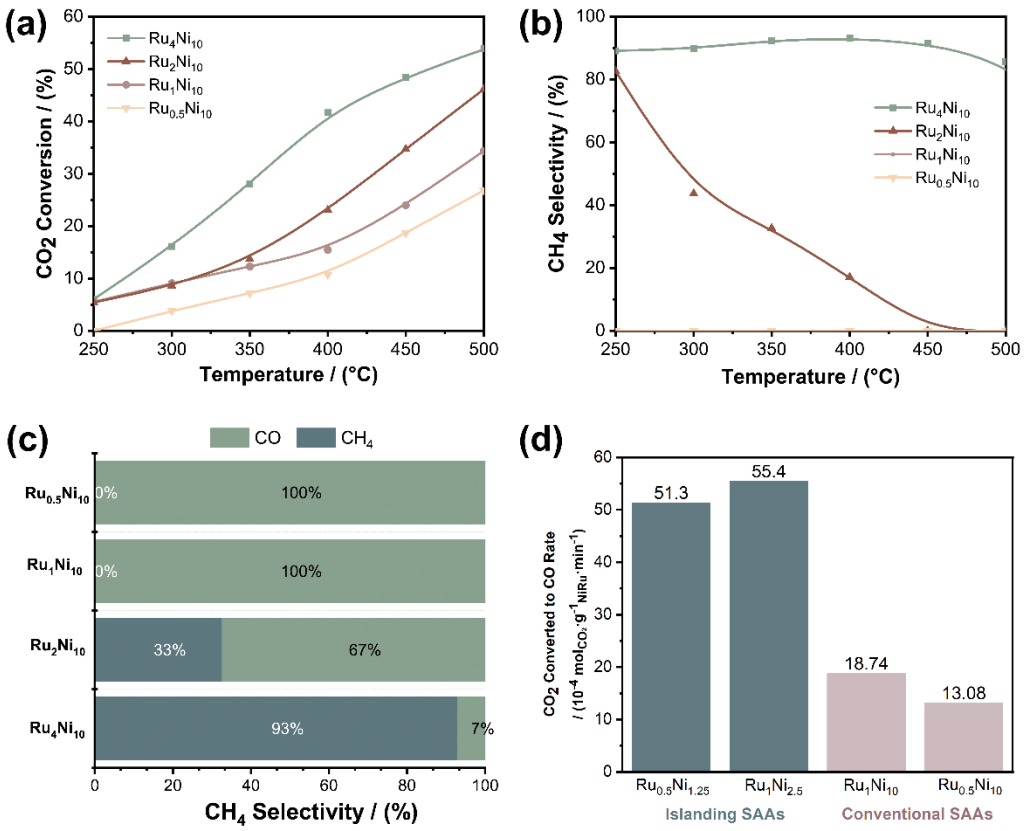


Fig. S15.

(a) The CO_2 conversion and (b) the CH_4 selectivity curves of Ru_xNi_{10}/TiO_2 (x=metal loading of Ru, x=0.5, 1, 2, 4) catalysts. (c) The product selectivity over Ru_xNi_{10}/TiO_2 (x=metal loading of Ru, x=0.5, 1, 2, 4) catalysts at 350 °C. (d) The CO_2 converted to CO rate over the single atom alloy (SAA) catalysts synthesized by the islanding effect strategy V.S. by conventional strategy.

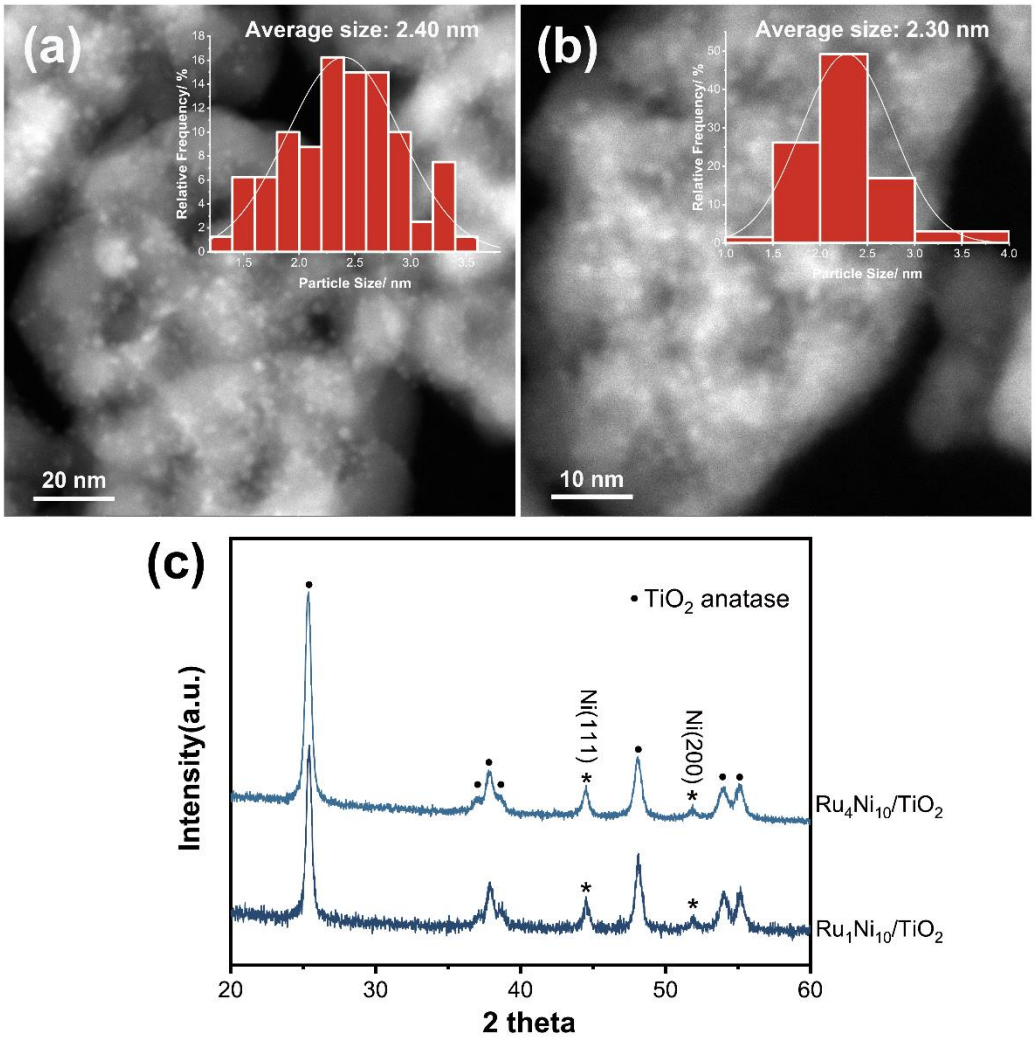


Fig. S16.

The particle size distribution and average size calculation of (a) Ru_4Ni_{10}/TiO_2 and (b) Ru_1Ni_{10}/TiO_2. (c) The XRD result of Ru_4Ni_{10}/TiO_2 and Ru_1Ni_{10}/TiO_2.

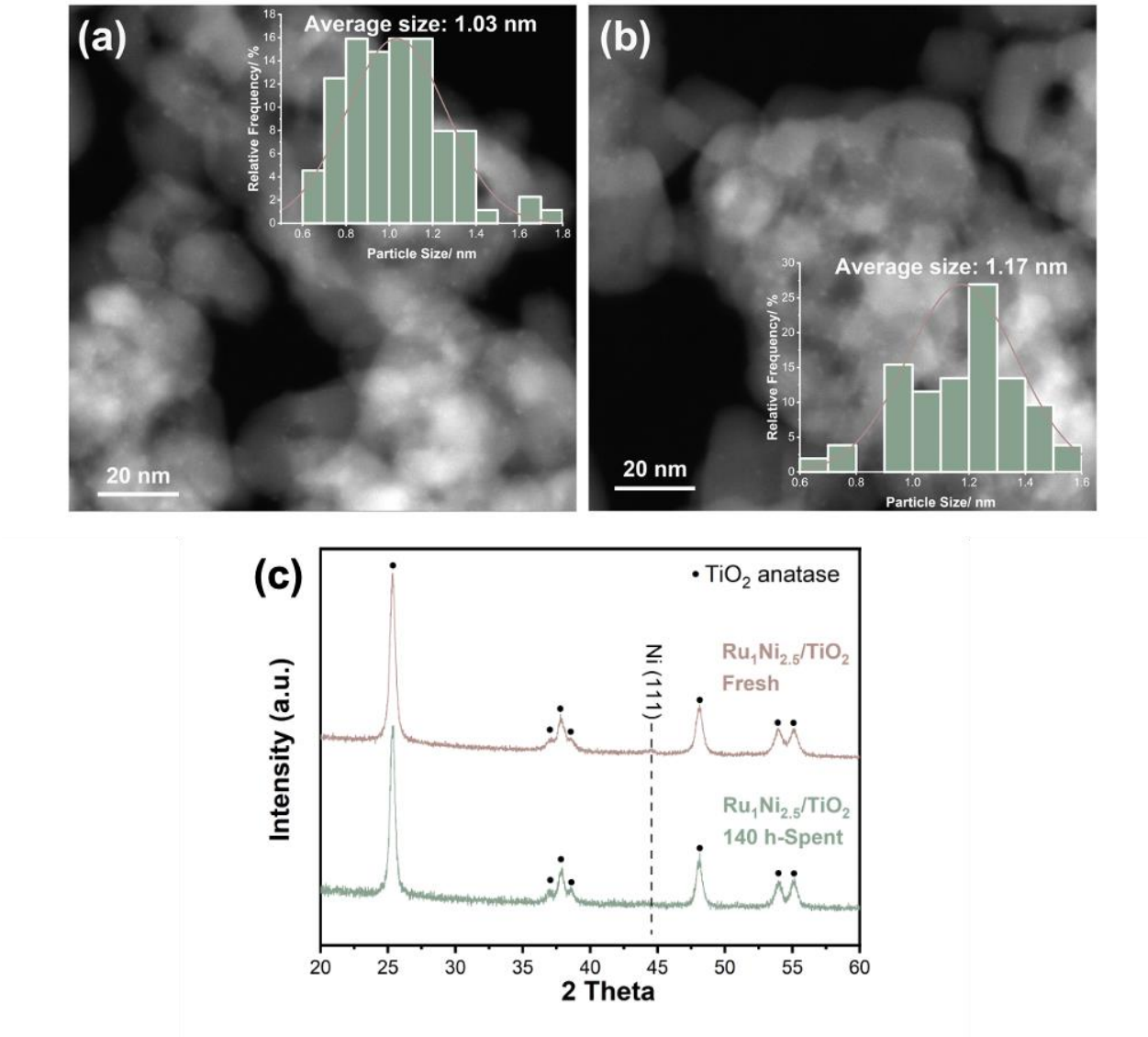


Fig. S17.

(a) The particle size distribution of the fresh $Ru_1Ni_{2.5}/TiO_2$ catalysts from STEM-HAADF image; (b) the particle size distribution of the after 140-h spent $Ru_1Ni_{2.5}/TiO_2$ catalysts from STEM-HAADF image. (c) XRD results of $Ru_1Ni_{2.5}/TiO_2$ before and after stability tests.

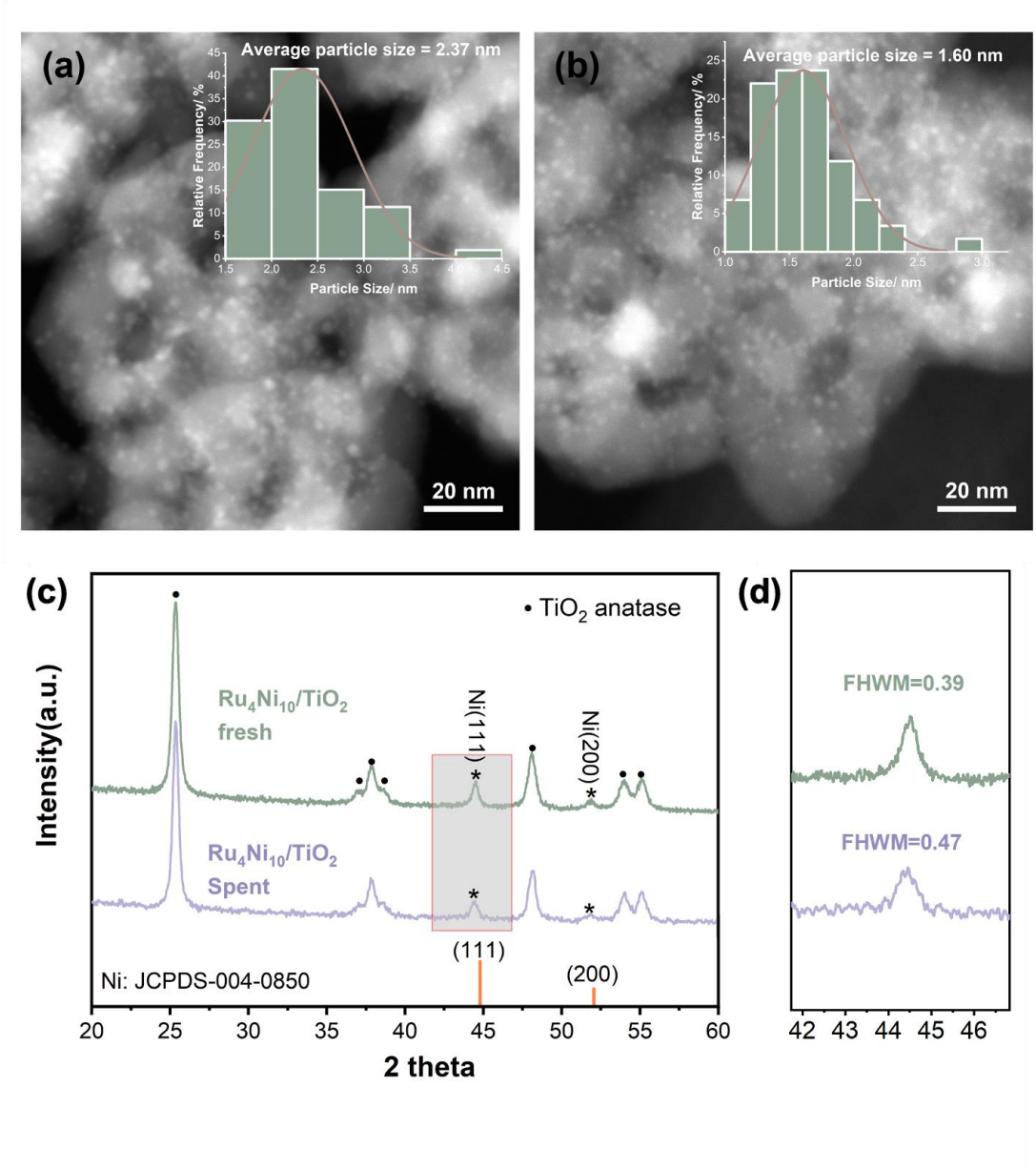


Fig. S18.

The morphology and size distribution calculation of Ru_4Ni_{10}/TiO_2 catalyst (a) before and (b) after long-term stability spent in STEM-HAADF. (c) XRD results of Ru_4Ni_{10}/TiO_2 before and after stability test. (d) Detailed line profile of the Ni (111) peak of the Ru_4Ni_{10}/TiO_2 before and after stability tests and the related full width at half maximum (FWHM) of the Ni (111) peaks.

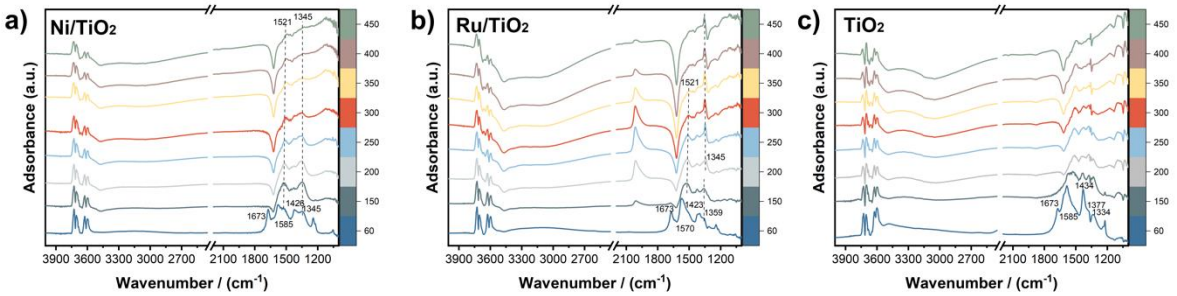


Fig. S19.

The CO_2 dissociation without H_2 on (a) Ni/TiO_2, (b) Ru/TiO_2, and (c) TiO_2.

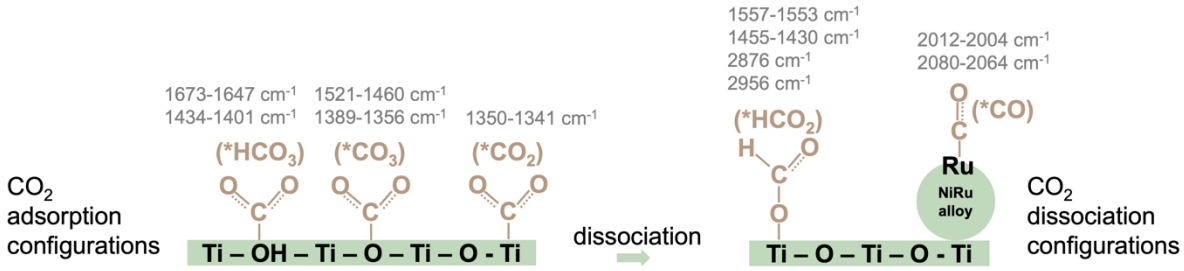


Fig. S20.

The CO_2 adsorption and dissociation configurations on Ru_xNi_y/TiO_2 catalysts.

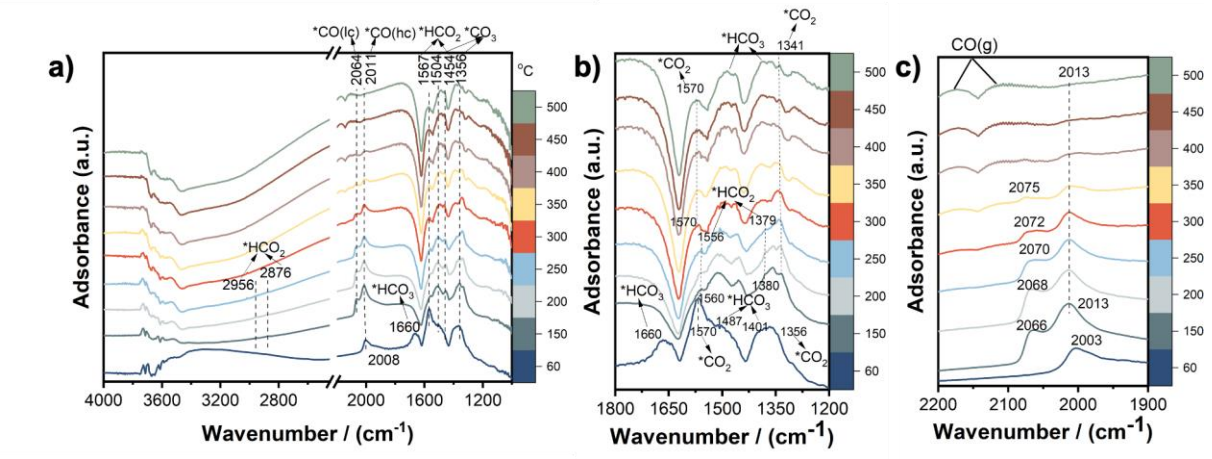


Fig. S21.

The steady-state in-situ DRIFTS experiments are conducted under the reaction conditions under the feed gas mixture (CO_2/H_2=1/4, balanced with N_2, total flow rate 60 sccm) flow at the temperature range from 60 to 500 °C: (a) $Ru_1Ni_{2.5}/TiO_2$ catalysts and the magnified (b) 1200-1800 cm^{-1} (c) 1900-2200 cm^{-1} regions.

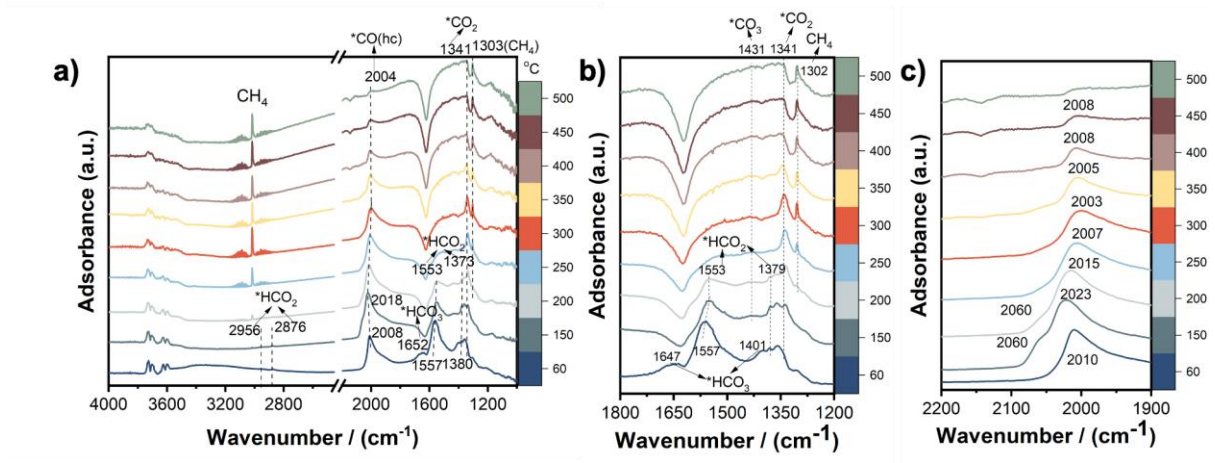


Fig. S22.

The steady-state in-situ DRIFTS experiments are conducted under the reaction conditions under the feed gas mixture (CO_2/H_2=1/4, balanced with N_2, total flow rate 60 sccm) flow at the temperature range from 60 to 500 °C: (a) Ru_4Ni_{10}/TiO_2 catalysts and the magnified (b) 1200-1800 cm^{-1} (c) 1900-2200 cm^{-1} regions.

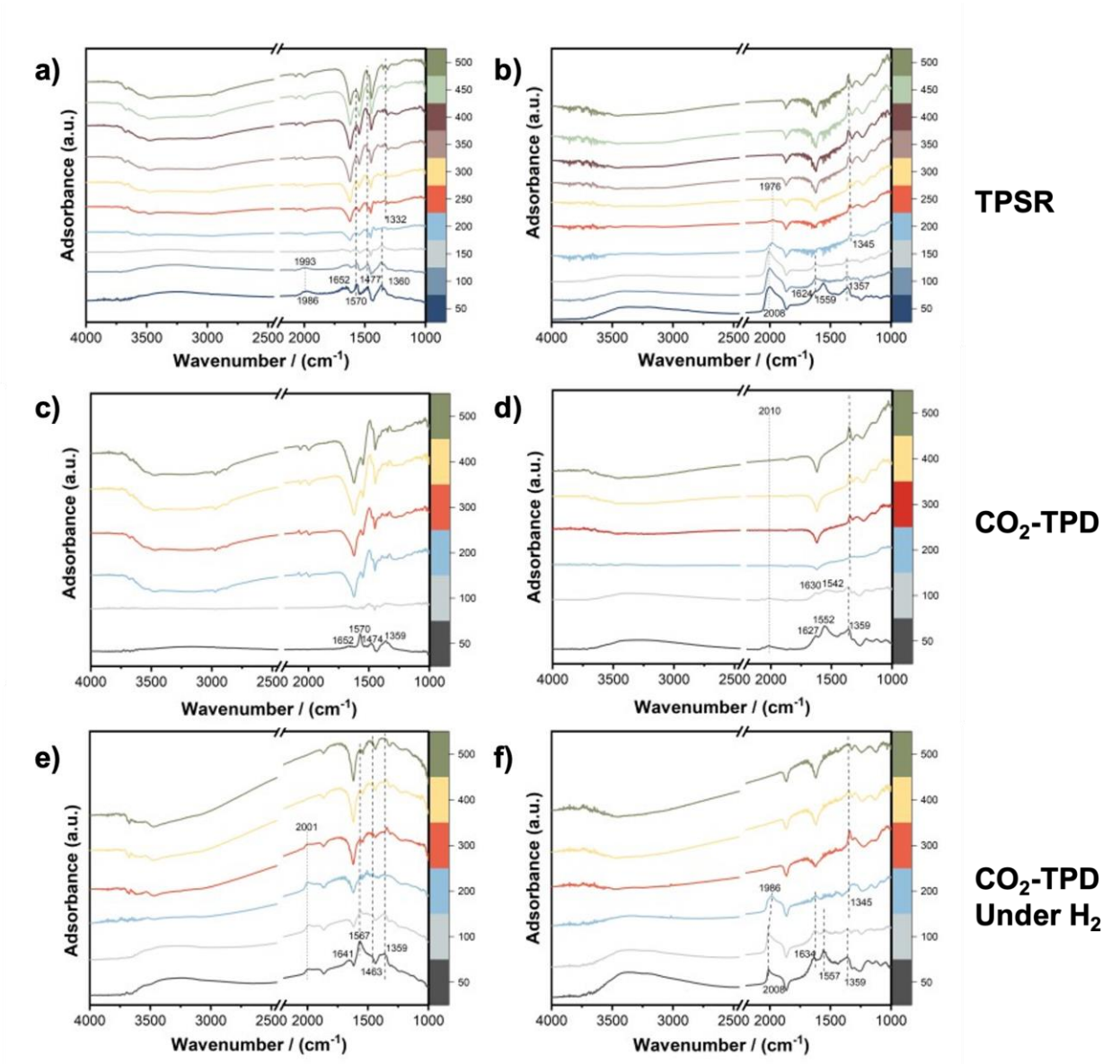


Fig. S23.

The TPSR results of (a) $Ru_1Ni_{2.5}/TiO_2$ and (b) Ru_4Ni_{10}/TiO_2 catalysts; the CO_2-TPD results of (c) $Ru_1Ni_{2.5}/TiO_2$ and (d) Ru_4Ni_{10}/TiO_2 catalysts; and the CO_2-TPD under H_2 results of (e) $Ru_1Ni_{2.5}/TiO_2$ and (f) Ru_4Ni_{10}/TiO_2 catalysts.

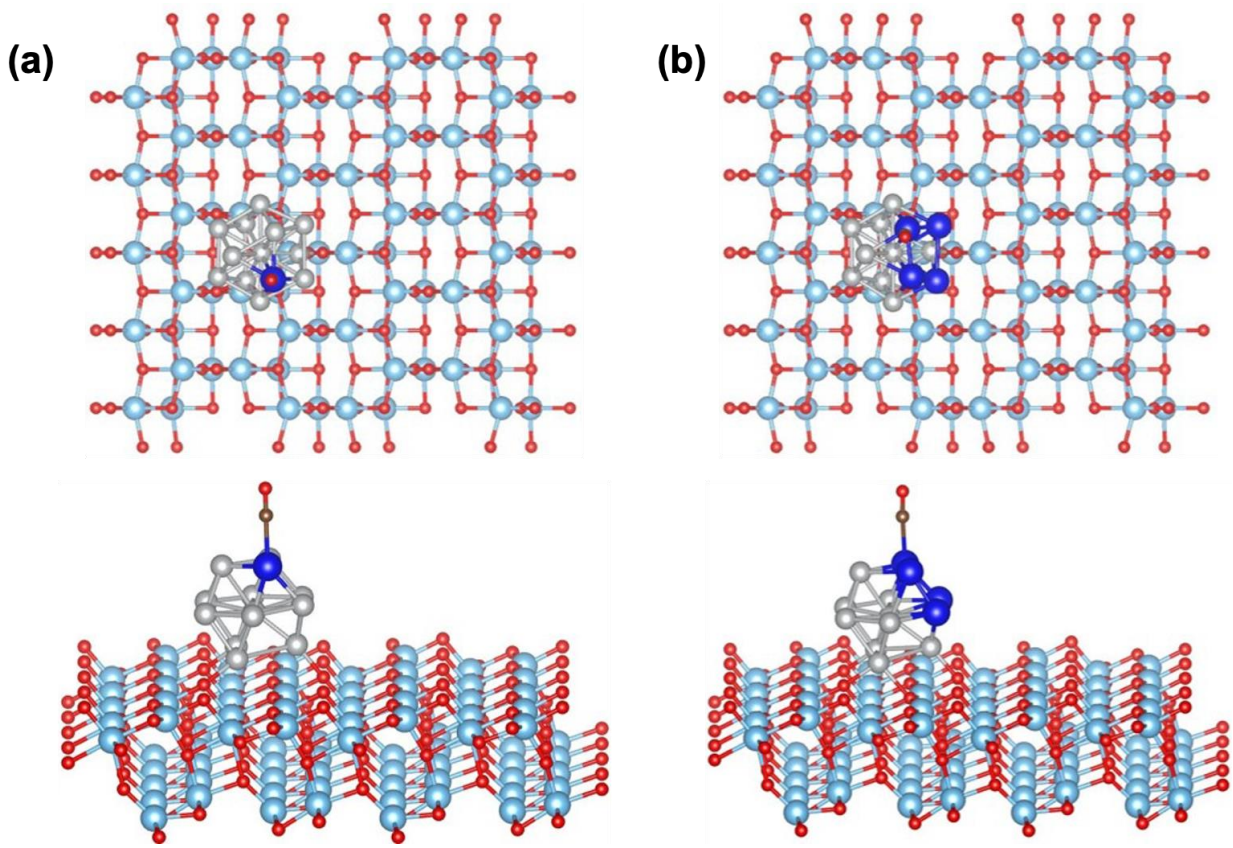


Fig. S24.

The schematic of simulated different Ru site on NiRu alloy catalysts with (a) cluster site and (b) single atom alloy site on Ni (111) plane.

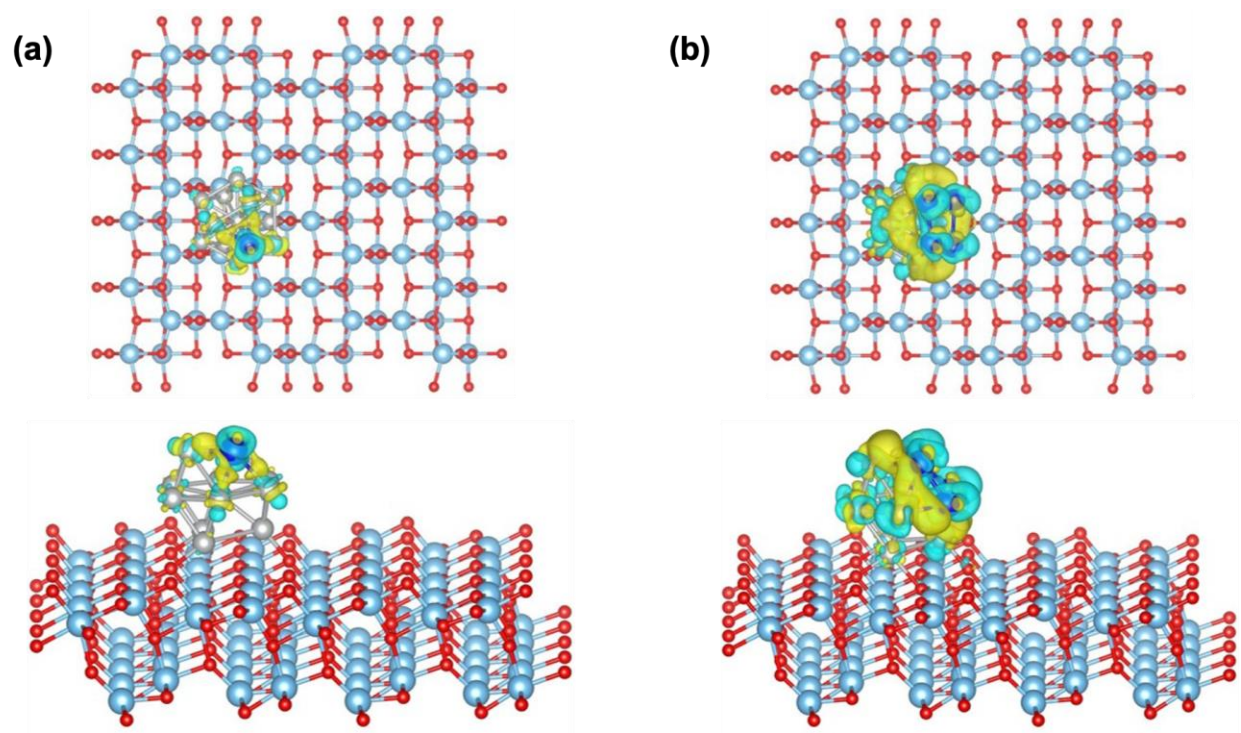


Fig. S25.

The charge density differences calculated by DFT of (a) Ru cluster site and (b) Ru single atom alloy site on NiRu alloy, where electrons are relocated from the yellow to the blue regions (Unit: 0.01 e/bohr^3).

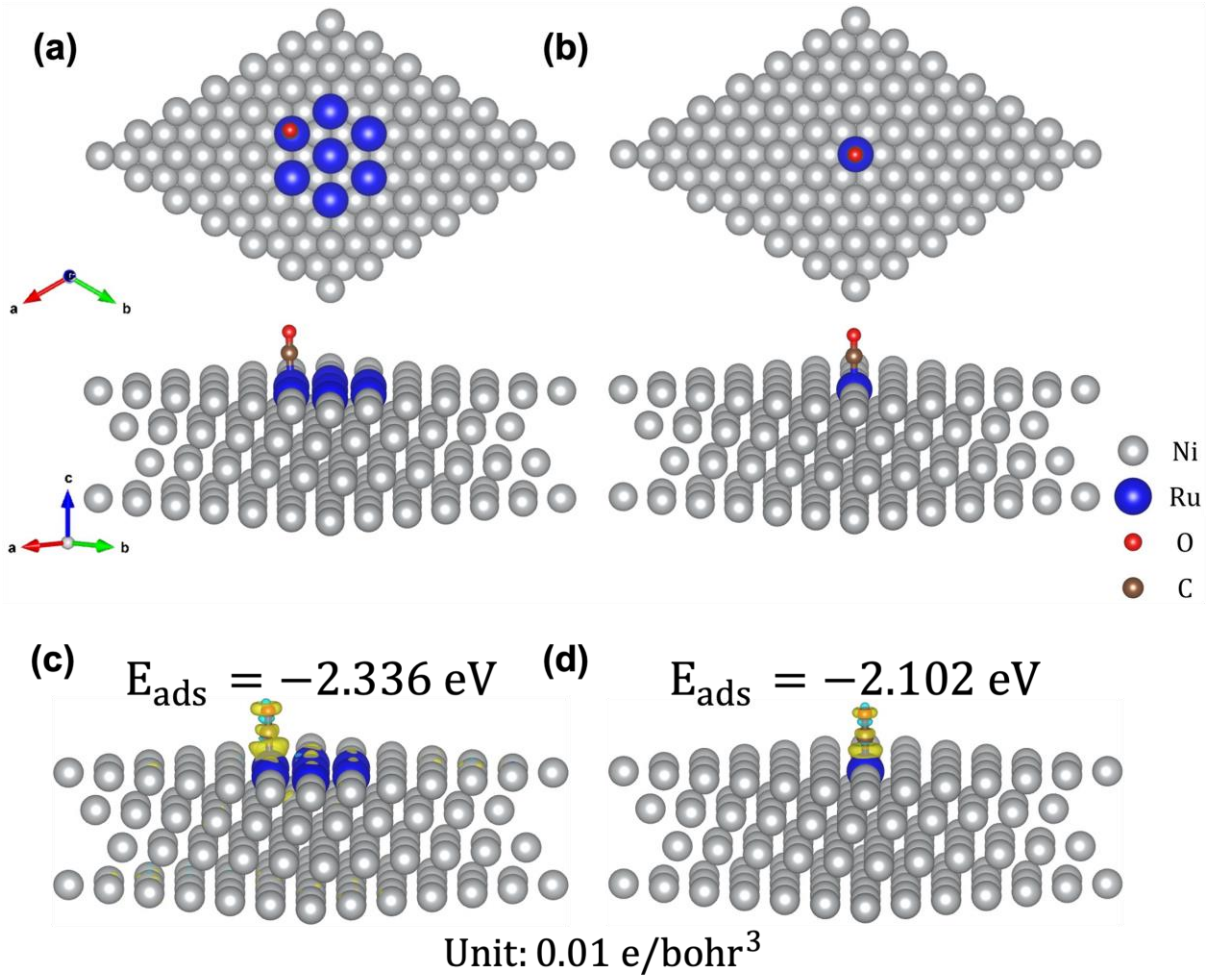


Fig. S26.

The atom-top site, which refers to the interaction of the adsorbed CO molecule with any vertex atom, is the most observed site in the in-situ CO-DRIFTS experiments, including linear adsorption, dicarbonyl adsorption and poycarbonyl adsorption configurations. The simulation on CO molecule with atom-top site on (a) Ru cluster site and (b) Ru single atom alloy site on Ni (111) plane.

Table S2.

The metallic ratio and reduction degree calculated by XPS results.

Sample	CO Selectivity (400 °C)[1]	NPs size[2]	Ru^0 % (Ru^0/Ru^0+Ru^{2+})[3]	Ni^0 % (Ni^0/Ni^0+Ni^{2+})[3]	Ru^0 binding energy/eV	Ni^0 binding energy/eV
$Ru_{0.5}Ni_{1.25}$	100 %	0.9 nm	69	27	280.24	853.33
$Ru_1Ni_{2.5}$	100 %	1.0 nm	66	24	280.13	853.45
Ru_2Ni_5	49.84 %	1.6 nm	67	24	280.18	853.48
$Ru_3Ni_{7.5}$	26.1%	2.0 nm	69	29	280.36	854.14
Ru_4Ni_{10}	6.84%	2.4 nm	65	25	280.31	853.31
$Ru_5Ni_{12.5}$	3%	3.2 nm	68	23	280.09	853.19

[1] Obtained from reaction tests results (in Fig. 1)

[2] Calculated from STEM-HAADF (the average size of 100 NPs)

[3] Calculated from XPS results:

Proportion of Ni^0=Area(Ni^0)/[Area(Ni^0)+ Area(NiO)+ Area($Ni(OH)_2$)]×100%

Proportion of Ru^0=Area(Ru^0)/[Area(Ru^0)+ Area(RuO_2)]×100%

Table S3.

Ru K-edge EXAFS fitting results of samples.

Samples	**Path**	**R(Å)**	**CN**	**σ^2 (10^{-3})**	**ΔE^0**	**R factor (%)**
Ru_4Ni_{10}/TiO_2	Ru-O	2.03±0.10	5.50±0.00	9.6	-0.83	0.04
	Ru-Ni	2.53±0.02	1.48±0.00	0.9	-0.83	0.04
	Ru-Ru	2.67±0.02	3.52±0.30	0.5	-0.83	0.04
$Ru_1Ni_{2.5}/TiO_2$	Ru-O-1	1.61±0.07	0.8±0.00	6.2	8.96	0.03
	Ru-O-2	1.91±0.07	1.50±0.00	6.2	8.96	0.03
	Ru-O-3	2.08±0.10	3.50±0.00	6.2	8.96	0.03
	Ru-Ni	2.54±0.03	0.54±0.30	3.2	8.96	0.03

Table S4.

The catalytic performance comparisons are made between catalysts in this work and the reported efficient catalysts for RWGS reaction.

Catalysts	**H_2:CO_2 ratio**	**Temperature / (°C)**	**CO formation rate /** ($\times 10^{-4} mol \cdot g_{cat}^{-1} s^{-1}$)	**CO_2 conversion / (%)**	**CO selectivity / (%)**	**Ref.**
$Ru_{0.5}Ni_{1.25}/TiO_2$	4:1	400	0.86	7	100	This work
$Ru_1Ni_{2.5}/TiO_2$	4:1	400	0.93	15	100	
Ru_2Ni_5/TiO_2	4:1	400	0.46	29	50	
Pt/TN-HN	3:1	400	0.79	10	97.6	[13]
Pt-Al_2O_3	1.4:1	400	0.016	38	N/A	[14]
Pt/TiO_2	4:1	400	0.15	25	96	[15]
Cu/SiO_2	4:1	600	0.09	8.3	100	[16]
Pt-CeO_2	1:1	400	0.29	15	99	[17]
Pt/CeO_2-AA-350	3:1	400	0.33	25	100	[18]
Pt/CeO_2-IMP-350	3:1	400	0.41	32	95	[18]
Pt NPs/Al_2O_3	3:1	400	1.26	8	90	[19]

Author contributions:

Conceptualization: SZ, JH

Experiment design: SZ

Data acquisition: SZ, XZ, HS, QG

Data analysis: SZ

DFT calculation: YL

Supervision: ARM, XL, JH

Writing – original draft: SZ

Writing – review & editing: ARM, XL, JH, SZ

Competing interests: Authors declare that they have no competing interests.

Data and materials availability: All data are available in the main text or the supplementary materials.

References

1 Mori, K., Miyawaki, K. & Yamashita, H. Ru and Ru–Ni Nanoparticles on TiO2 Support as Extremely Active Catalysts for Hydrogen Production from Ammonia–Borane. *ACS Catalysis* **6**, 3128-3135 (2016). https://doi.org:10.1021/acscatal.6b00715

2 Wang, Z. *et al.* CO-tolerant RuNi/TiO2 catalyst for the storage and purification of crude hydrogen. *Nature Communications* **13**, 4404 (2022). https://doi.org:10.1038/s41467-022-32100-x

3 Zou, S. *et al.* Structure-performance correlation on bimetallic catalysts for selective CO2 hydrogenation. *Energy & Environmental Science* (2023). https://doi.org:10.1039/D3EE01650A

4 Hashimoto, N., Mori, K. & Yamashita, H. In Situ Investigation on the Formation Mechanism of High-Entropy Alloy Nanoparticles Induced by Hydrogen Spillover. *The Journal of Physical Chemistry C* **127**, 20786-20793 (2023). https://doi.org:10.1021/acs.jpcc.3c05375

5 Li, Z. *et al.* Well-Defined Materials for Heterogeneous Catalysis: From Nanoparticles to Isolated Single-Atom Sites. *Chemical Reviews* **120**, 623-682 (2020). https://doi.org:10.1021/acs.chemrev.9b00311

6 Liu, L. & Corma, A. Bimetallic Sites for Catalysis: From Binuclear Metal Sites to Bimetallic Nanoclusters and Nanoparticles. *Chemical Reviews* **123**, 4855-4933 (2023). https://doi.org:10.1021/acs.chemrev.2c00733

7 Newville, B. R. a. M. ATHENA, ARTEMIS, HEPHAESTUS: data analysis for X-ray absorption spectroscopy using IFEFFIT. *Journal of Synchrotron Radiation* **12**, 537-541 (2005). https://doi.org:https://doi.org/10.1107/S0909049505012719

8 Kohn, W. & Sham, L. J. Self-Consistent Equations Including Exchange and Correlation Effects. *Physical Review* **140**, A1133-A1138 (1965). https://doi.org:10.1103/PhysRev.140.A1133

9 Kresse, G. & Furthmüller, J. Efficiency of ab-initio total energy calculations for metals and semiconductors using a plane-wave basis set. *Computational Materials Science* **6**, 15-50 (1996). https://doi.org:https://doi.org/10.1016/0927-0256(96)00008-0

10 Perdew, J. P., Burke, K. & Ernzerhof, M. Generalized Gradient Approximation Made Simple. *Physical Review Letters* **77**, 3865-3868 (1996). https://doi.org:10.1103/PhysRevLett.77.3865

11 Grimme, S. Semiempirical GGA-type density functional constructed with a long-range dispersion correction. *Journal of Computational Chemistry* **27**, 1787-1799 (2006). https://doi.org:https://doi.org/10.1002/jcc.20495

12 Kresse, G. & Joubert, D. From ultrasoft pseudopotentials to the projector augmented-wave method. *Physical Review B* **59**, 1758-1775 (1999). https://doi.org:10.1103/PhysRevB.59.1758

13 Chen, Z. *et al.* Reciprocal regulation between support defects and strong metal-support interactions for highly efficient reverse water gas shift reaction over Pt/TiO2 nanosheets catalysts. *Applied Catalysis B: Environmental* **298**, 120507 (2021). https://doi.org:https://doi.org/10.1016/j.apcatb.2021.120507

14 Kim, S. S., Lee, H. H. & Hong, S. C. A study on the effect of support's reducibility on the reverse water-gas shift reaction over Pt catalysts. *Applied Catalysis A: General* **423-424**, 100-107 (2012). https://doi.org:https://doi.org/10.1016/j.apcata.2012.02.021

15 Torres-Sempere, G. *et al.* Subnanometric Pt clusters dispersed over Cs-doped TiO2 for CO2 upgrading via low-temperature RWGS: operando mechanistic insights to guide an optimal catalyst design. *Journal of Materials Chemistry A* **12**, 1779-1792 (2024). https://doi.org:10.1039/D3TA05482A

16 Chen, C.-S., Cheng, W.-H. & Lin, S.-S. Enhanced activity and stability of a Cu/SiO2 catalyst for the reverse water gas shift reaction by an iron promoter. *Chemical Communications*, 1770-1771 (2001). https://doi.org:10.1039/B104279N

17 Chen, X. *et al.* Identification of relevant active sites and a mechanism study for reverse water gas shift reaction over Pt/CeO2 catalysts. *Journal of Energy Chemistry* **25**, 1051-1057 (2016). https://doi.org:https://doi.org/10.1016/j.jechem.2016.11.011

18 Zhao, Z. *et al.* Atomically dispersed Pt/CeO2 catalyst with superior CO selectivity in reverse water gas shift reaction. *Applied Catalysis B: Environmental* **291**, 120101 (2021). https://doi.org:https://doi.org/10.1016/j.apcatb.2021.120101

19 Kobayashi, D. *et al.* Boosting reverse water-gas shift reaction activity of Pt nanoparticles through light doping of W. *Journal of Materials Chemistry A* **9**, 15613-15617 (2021). https://doi.org:10.1039/D1TA03480D